



**Self-assembled Gold Nanorime Mesh Conductors for
Invisible Stretchable Supercapacitor**

Journal:	<i>Nanoscale</i>
Manuscript ID	NR-COM-05-2018-004256.R2
Article Type:	Communication
Date Submitted by the Author:	06-Aug-2018
Complete List of Authors:	Wang, Yan; Monash University, chemical engineering Gong, Shu; Monash University, Department of Chemical Engineering Dong, Dashen; Monash University, Department of Chemical Engineering Zhao, Yunmeng; Monash University, Department of Chemical Engineering Yap, Lim Wei; Monash University, Chemical Engineering Shi, Qianqian; Monash University, Department of Chemical Engineering An, Tiance; Monash University, Department of Chemical Engineering Ling, Yunzhi; Monash University, Department of Chemical Engineering Simon, George; Monash University, Materials Science and Engineering Cheng, Wenlong; Monash University, Department of Chemical Engineering



Nanoscale

COMMUNICATION

Self-assembled Gold Nanorime Mesh Conductors for Invisible Stretchable Supercapacitor

Yan Wang^{a,b}, Shu Gong^{a,b}, Dashen Dong^{a,b}, Yunmeng Zhao^{a,b}, Lim Wei Yap^{a,b}, Qianqian Shi^{a,b}, Tiance An^{a,b}, Yunzhi Ling^{a,b}, George. P. Simon^{b,d}, Wenlong Cheng^{a,b,c}

Thin, skin-conformal, transparent and stretchable energy devices are ideal for powering future wearable and implantable electronics. However, it is difficult to achieve such “unfeeling” and “invisible” devices with traditional materials and design methodologies because of the challenge of simultaneously achieving high optical transparency, high electrical conductivity and high mechanical stretchability. Here, we report a two-step nanowire growth approach to fabricate gold nanorime mesh conductors, enabling skin-thin, transparent and stretchable supercapacitors. Solution-state oleylamine-capped 2-nm-thin gold nanowires self-assemble into highly transparent nanomeshes, which then serve as templates to grow highly conductive vertically aligned nanowires. This two-step solution-plus-surface nanowire growth strategy leads to elastic gold nanorime mesh conductors with an optical transparency up to 90.3% at 550 nm, a low sheet resistance as low as $1.7 \pm 0.8 \Omega \text{ sq}^{-1}$, and a stretchability of over 100% strain. Such elastic conductors are successfully used to construct symmetrical supercapacitors that can simultaneously achieve high areal capacitance and high stretchability, demonstrating the potential to power future bio-integrateable electronics.

Received 00th January
20xx,
Accepted 00th January
20xx
DOI: 10.1039/x0xx00000x
www.rsc.org/

Introduction

Next-generation electronics should be ultrathin, elastic and curved¹ with Young's moduli matching human skins or muscles so that it can be seamlessly integrated to become parts of human body. Ideally, they may be also transparent to realize our ultimate dream of 'unseeable' and 'unfeeling' wearable/implantable biondiagnostics anytime anywhere². Importantly, energy devices will be critical components of such an invisible bio-integrateable system, which ideally should be thin and lightweight, whilst also mechanically soft and optically transparent.

Encouragingly, past several years have witnessed significant advances in developing stretchable energy devices³ using two viable strategies – structures that stretch (STS) or materials that stretch (MTS)¹. With either STS or MTS or both, a number of stretchable energy generation and storage devices⁴, including batteries⁵, supercapacitors^{6, 7}, photovoltaics⁸, triboelectricity⁹ and

thermoelectrics¹⁰ have been reported. However, it is rare to achieve three important features, ultrathin, stretchable and transparent simultaneously. This is because high conductivity usually requires the deposition of a large amount of active materials, which typically lead to thick films with reduced optical transparency and mechanical stretchability. As far as electrochemical capacitors (namely, supercapacitors) are concerned, active materials including carbon nanotube (CNT)^{6, 11}, graphene¹²⁻¹⁴, metal nanowires^{15, 16} and conducting polymers¹⁷ have been used for constructing supercapacitor electrodes. However, it remains challenging to combine high mechanical stretchability, optical transparency and high capacitance performance, all within a skin-thin format with existing materials and processing technologies¹⁸⁻²⁰.

Herein, we present an entirely solution-based, two-step nanowire-on-nanowire growth strategy to fabricate self-assembled nanorime mesh conductors for skin-thin, stretchable and transparent supercapacitors. Such prepared mesh electrodes can reach an electrical conductivity of $1.7 \pm 0.8 \Omega \text{ sq}^{-1}$ and an optical transparency of 90.3% at 550 nm wavelength. This allows for fabrication of symmetrical supercapacitors with overall thickness of $\sim 100 \mu\text{m}$ yet stretchable up to 100% strain with capacitance retention of $\sim 76\%$. In addition, the as-received supercapacitor exhibits superior mechanical flexibility under repeated stretching (0-100% strain) and bending (0-180 degree) cycling.

^a Department of Chemical Engineering, Monash University, Clayton, Victoria 3800, Australia; Email: wenlong.chena@monash.edu

^b New Horizon Research Centre, Monash University, Clayton, Victoria 3800, Australia;

^c The Melbourne Centre for Nanofabrication, Clayton, Victoria 3800, Australia;

^d Department of Materials Science and Engineering, Monash University, Clayton, Victoria 3800, Australia;

† Electronic Supplementary Information (ESI) available: Experimental section, supporting figures and videos. See DOI: 10.1039/x0xx00000x

Results and discussion

Fabrication and Characterization of Gold Nanorime Mesh Conductors

Fig. 1a-d illustrates the fabrication process of self-assembled nanorime mesh conductors. The 2 nm-thin oleylamine-capped gold nanowires were synthesized^{21, 22}, which were then stored under room temperature for a certain period of time (ageing process) before drop casting onto air/water interface. In our previous paper²³, we have demonstrated that oleylamine ligands will gradually desorb from nanowire surface during the ageing process. Drop-casting of the aged nanowire solution onto air/water interface can lead to self-assembled nanomesh (Fig. 1a). By controlling the ageing time, we can adjust the conductivity and optical transparency of the mesh conductors²³. The mesh structures were robust to be transferred onto elastomeric substrates (Fig. 1b). The as-obtained meshes only possessed a sheet resistance of about $130.1 \Omega \text{ sq}^{-1}$ with limited electroactive surface areas. We could further convert the bundled nanowire meshes into nanorime meshes. An O_2 plasma was intermediately applied to remove surface-bonding oleylamine ligands after transferring process, leading to fusion/fragmentation of nanowires (Fig. 1c). Interestingly, these plasma-treated nanowire structures could serve as seeds to

enable site-selective growth of highly aligned nanowire arrays only on mesh templates (Fig. 1d), simply by electroless plating by immersing nanomesh templates into growth solution containing gold precursors, 4-Mercaptobenzoic acid (MBA) and reducing agents. Surface enhanced Raman results show that MBA molecules are present on the nanowire surfaces (Fig. S1).

This facile process is entirely wet-chemistry-based, without the need of any additional expensive equipment, yet is able to achieve large-scale uniform transparent conductor (Fig. 1e). Scanning electron microscopy (SEM) characterisations demonstrate the transition of nanomesh from nanowire bundles (Fig. 1f) to fused/fragmented nanowires (Fig. 1g) and to highly aligned nanowire arrays grown in the normal directions forming nanorimes (Fig. 1h). The densely packed nanowire arrays prevented from the electron beam penetration, hence, it is impossible to observe individual nanowire packing using transmission electron microscopy (TEM). However, nanorime structures are clearly observed in the edge area (Fig. S2 in ESI†).

We found that MBA plays a critical role in forming nanorimes in the gold plating step (Fig. 1c to Fig. 1d). In the absence of MBA in the growth solution, no nanorime structures were obtained. High concentration (1.96 mM) of MBA will result in disordered nanowire

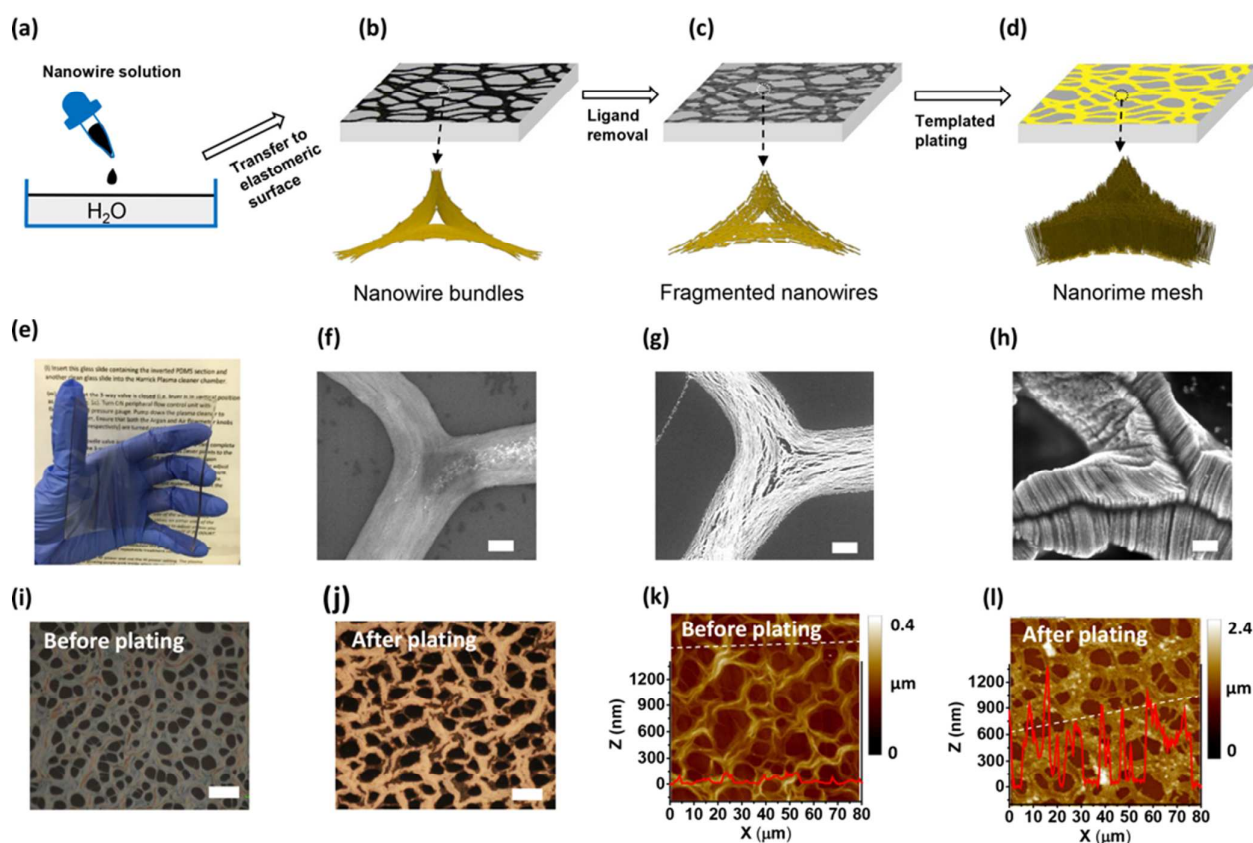


Fig. 1 Fabrication and characterization of nanorime mesh conductors. (a) Drop-casting of oleylamine-capped 2-nm-thin gold nanowire solution onto the air-water interface, leading to the formation of self-assembled nanomesh; (b) Bundled nanowire mesh transferred onto elastomeric transparent substrate; (c) Removal of oleylamine by O_2 plasma treatment, leading to fused and fragmented nanowires; (d) Nanomesh-templated aligned gold nanowire arrays in the normal directions, leading to the formation of nanorime mesh. (e) A typical photograph of the as-prepared 10×10 cm gold nanorime mesh conductor on PDMS. (f-h) SEM images of nanomesh structures of 2-nm-thin nanowire bundles (f), fused/fragmented nanowires (g), and gold nanorimes after templated gold plating (h). Scale bar: 200 nm. (i-j) Optical micrographs of nanomeshes before and after gold plating. Scale bar: 20 μm . (k-l) Atomic force microscopy (AFM) images of nanomeshes before and after gold plating. Red lines correspond to line scan profile of white dashed lines. $t_p = 20$ mins, $t_A = 3$ hrs and $t_G = 9$ mins.

growth at the margin area of nanowire bundles, while lower concentrations (e.g. 0.49 mM and 0.25 mM) will end up with either thicker nanowires or larger gold particles respectively (Fig. S3 in ESI[†]). Nevertheless, finely aligned nanowire arrays could be achieved with 0.98 mM MBA. Longer growth time led to longer and denser nanowires (Fig. S4 in ESI[†]). A panoramic view of nanorime meshes is shown in Fig. S5 in ESI[†], clearly demonstrating the site-specificity of growth of aligned gold nanowires in the gold plating step. In the entire process, mesh-like structures could be well-maintained as shown in the optical characterization (Fig. 1i, j) and atomic force microscopy (AFM) characterization (Fig. 1k, l). The AFM line scan analysis shows that the height of nanomesh increased from 110 nm \pm 45 nm to 1008 nm \pm 114 nm before and after seed-mediated nanowire growth.

Apparently, the growth mechanism of our vertical nanowire arrays is similar to that of the gold nanoforest where surface-bonded spherical seeds were used²⁴. In our case, fused/fragmented nanowires served as active sites for vertical nanowire growth. In the plasma treatment step, it is likely that weak-bonding oleylamine ligands were fully removed and fused/fragmented nanowires formed. In the growth solution, strong-binding MBA may quickly anchor on the fused/fragmented nanowires to facilitate nanowire arrays growth. This growth mechanism is further proved by our success in growing suspended nanorime web using free-standing oleylamine-capped nanowire bundles supported by micro-pillared PDMS surfaces (Fig. S6 in ESI[†]). The plasma treatment could only remove the oleylamine ligands from outside of the bundles, where the resulted fused/fragmented nanowires served as active sites for

gold deposition, hence, promoting growth of vertical nanowire arrays.

Our nanorime formation process shares the similarity to other multiscale hierarchical configurations of nanowire growth reported by Ko *et al.*²⁵⁻²⁹. The difference is that our system is not heterogeneous junction but gold-gold junction. In the control experiment with evaporated gold nanoparticles as seeds, we failed to obtain nanorime structures (Fig. S7 in ESI[†]). This could be because of strong interfacial bonding between evaporated gold nanoparticles and elastomer surface, preventing from nucleation and growth at the interface.

Key parameters governing electrical conductivity and optical transparency

We systemically investigated how the three key parameters, namely ultrathin nanowire ageing time (t_A), plasma treatment time (t_P) and seed-mediated nanowire growth time (t_G), influenced conductivity and transparency of gold nanorime mesh conductors. Usually it was found that long, initial plasma treatment time enhanced the optical transparency but with increased sheet resistance, as shown for the particular sample with $t_A = 9$ hrs, $t_G = 6$ mins (Fig. S8a-b in ESI[†]).

Without plasma treatment, gold nanostructures grew both in the mesh and vacant areas (SEM and microscopic characteristics in Fig. S8c, e, g, ESI[†]), leading to an almost optically-opaque film (transmittance < 2%) with a very low sheet resistance of 1.78 \pm 0.9 Ω sq⁻¹. With plasma treatment, seed-mediated nanowire growth

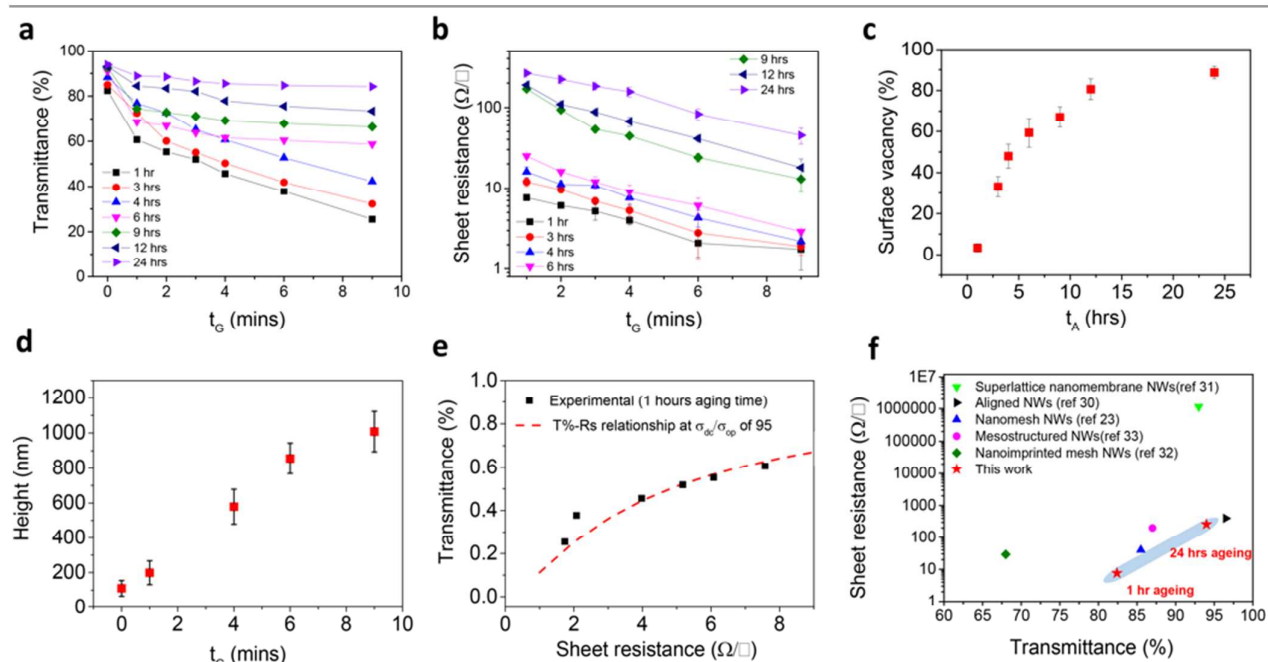


Fig. 2 (a) Optical transmittance ($\lambda = 550$ nm) as a function of templated nanowire growth time t_G and for different nanomeshes obtained with different ageing time t_A . (b) Sheet resistance as a function of templated nanowire growth time t_G for different nanomeshes obtained with different ageing time t_A . (c) Nanowire film surface voidage as a function of different ageing time t_A . (d) The change of nanowire height measured by AFM as a function of templated nanowire growth time t_G . (e) Experimentally measured optical transmittance ($\lambda = 550$ nm) as a function of sheet resistance (scattered plot). Red dashed line is the numerical fitting. (f) Comparison between this work and literature reports. Data points are extracted from the following papers: Green down triangle, self-assembled superlattice nanomembrane NWs — the study by Cheng *et al.* (31); Dark right triangle, self-aligned NW monolayers — the study by Correa-Duarte *et al.* (30); Magenta circle, mesostructure templated thin Ag-AuNWs — the study by Markovich *et al.* (23); Blue up triangle, self-assembled nanomesh NWs — the study by Cheng *et al.* (33); Olive diamond, templated mesh NWs by nanoimprinting — the study by Kraus *et al.* (32); red filled star, this study.

was site-selective to nanomesh areas, as can be seen in SEM and microscopic images in Fig. S8d, f, h, ESI†. This substantially enhanced optical transparency (68% transmittance), albeit with increased sheet resistance ($12.5 \pm 1.5 \Omega \text{ sq}^{-1}$). We will then choose $t_p=20$ mins for transparent conductor fabrication in this work.

We varied both t_A from 1 to 24 hrs and t_G from 1 to 9 minutes to see how they would affect optical transparency (Fig. 2a) and electrical conductivity (Fig. 2b). Consistent with our previous report, the increased ageing time would lead to larger pore sizes and thicker bundles (Microscopic images in Fig. S9a-g, ESI†, for t_G from 1 to 24 hrs). As a result, surface vacant areas increased up to about 80% after 24 hrs ageing (Fig. 2c). Since large pores favour light transmittance and thick nanobundles promote electrical conductivity, increased ageing time t_G will lead to higher transparency and lower conductivity. The seed-mediated nanowire growth reduced further in optical transmittance as a result of nanowire deposition (Fig. S9h-n in ESI†). This can be demonstrated by AFM studies featuring surface morphology before and after densely-aligned nanowire arrays growth, for different periods of time (1, 4, 6 and 9 mins) at $t_G=3$ hrs (Fig. S10 in ESI†), the scan line in Fig. 2d shows gradually increased bundle thickness, whilst increasing nanowire growth time. In particular, with 24 hrs ageing time, the nanowire mesh electrode has a transparency of >84.2% over a wide range of spectral window from 300 to 800 nm even for long seed-mediated nanowire growth time, $t_G = 9$ mins (Fig. S11 in ESI†). With shortest ageing time ($t_A = 1$ hr) in this study and longest seed-mediated growth time ($t_G = 9$ minutes), we could reach a

sheet resistance as low as $1.7 \pm 0.8 \Omega \text{ sq}^{-1}$.

Figure of merit (FOM) is usually a measure of performance of transparent conductor, which is the ratio of optical conductivity, $\sigma_{op}(\lambda)$ and direct current conductivity, σ_{dc} . FOM can be determined by fitting the following equation:

$$T(\lambda) = \left(1 + \frac{188.5 \sigma_{op}(\lambda)}{R_{sh} \sigma_{dc}} \right)^{-2}$$

where $R_{sh}(\lambda)$ is sheet resistance of transparent conductor. By numerically fitting the experimental data, FOM values can be estimated for the gold nanorime mesh conductor (Fig. 2e, Fig. S12 in ESI†). At the wavelength of 550 nm, we obtained a FOM of 95 for $t_A = 1$ hr, which is more than three times greater than the previous mesh nanowire membrane-based transparent electrode²³. This nanorime mesh conductor stands out while comparing to other gold nanowire based transparent electrodes^{23,30-33} (Fig. 2f).

For further investigation, we compared the stability of the gold nanorime mesh conductor to the bundled nanowire mesh-only electrode. For the mesh-only transparent electrode, the conductivity was permanently lost after 65 days storage at room temperature (Fig. S13a-c in ESI†), which was due to Rayleigh instability of oleylamine-capped ultrathin gold nanowires causing their break down into discrete particles. In contrast, the nanomesh-templated transparent electrode did not show any obvious morphology change, with negligible resistance variation during the same storage conditions (Fig. S13d-f in ESI†).

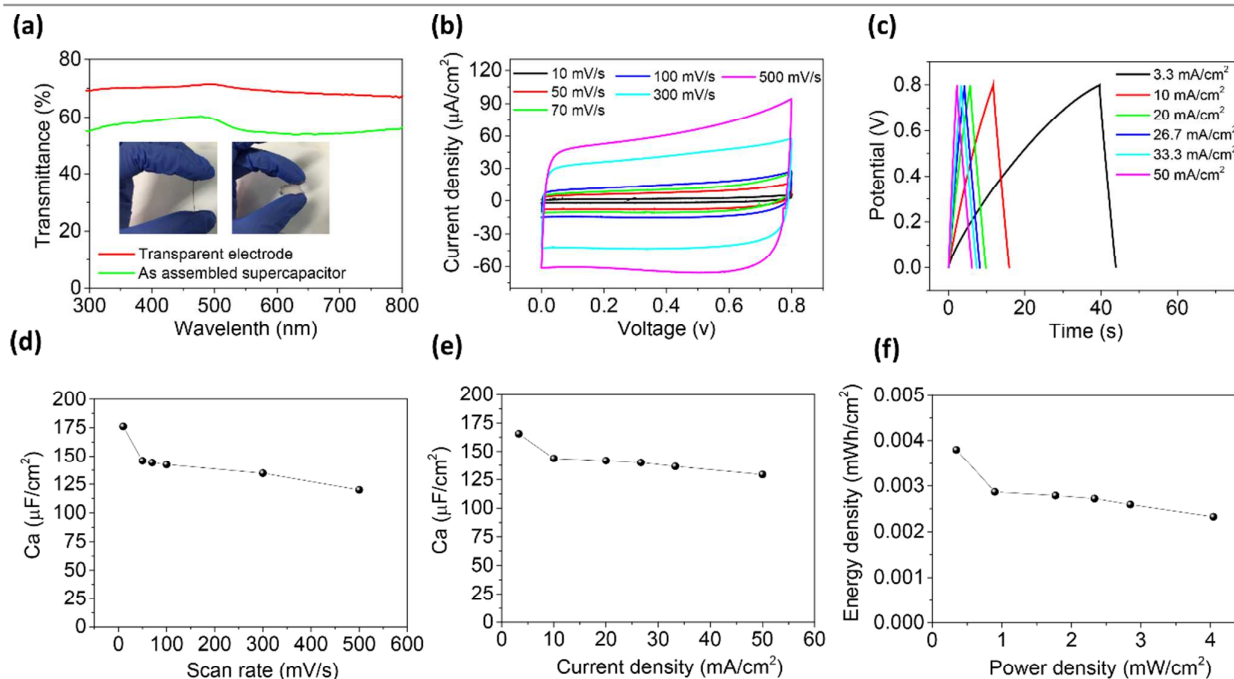


Fig. 3 Transparent supercapacitor based on gold nanorime mesh conductors. $t_p=20$ mins, $t_A=9$ hrs and $t_G=9$ mins. (a) Optical transmittance of the nanorime electrode and assembled symmetrical supercapacitor. The inset images show flexibility of as prepared transparent supercapacitor. (b) Cyclic voltammetry (CV) curves of the supercapacitors at various scan rates from 10 mV/s to 500 mV/s. (c) Galvanostatic charging-discharging (GCD) curves of the supercapacitors at a constant current of 3.3 mA, 10 mA, 20 mA, 26.7 mA, 33.3 mA and 50 mA. (d) The calculated areal capacitances of the supercapacitor using CV curves in (b). (e) The calculated areal capacitances of the supercapacitor using GCD curves in (c). (f) Areal power density/energy density of the supercapacitor.

Mechatronic properties

To study the electromechanical properties of the transparent gold nanorime conductor, we examined the stretchability of the electrodes with varied ageing time (Fig. S14a, ESI[†], t_p , 20 mins t_G , 9 mins). For $t_A = 1$ hr, the conductivity was lost when the film was stretched to $\sim 127\%$ strain; however, for $t_A = 24$ hrs, the stretchability limit reduced to $\sim 51\%$ strain. This result was expected because shorter ageing time gives rise to thinner nanowire bundles, which lead to better stretchability, consistent with the bending stiffness theory³⁴.

For the sample with $t_p = 20$ mins, $t_A = 9$ hrs and $t_G = 9$ mins, a good compromise was achieved among stretchability (100%), sheet resistance ($R_{sh} = 6.4 \pm 0.5 \Omega \text{ sq}^{-1}$) and transparency (66.7%). We found a resistance only increased by a factor of 5 even under large strain (80%) (Fig. S14b in ESI[†]). Dynamic conductivity change can be seen in Fig. S14c in ESI[†]. In addition, the electrodes also exhibited excellent durability with stable electrical responses to 50 stretching/releasing cycles under 100% strain (Fig. S14d in ESI[†]). Noted that the traditional solid gold film and the mesh film without nanowire structures could only be stretched to 10% and 22% respectively, before losing conductivity (Fig. S15 in ESI[†]). Remarkably, the gold nanorime meshes could also be fabricated directly on the conventional scotch tape to achieve 'invisible' conductive tape. The brightness of the LED light maintained the same when the tape was under large, repeated deformation (Fig. S16 and Movie S1 in ESI[†]). This demonstration indicated the

prospect of this electrode for versatile transparent and stretchable wearable energy devices, such as supercapacitors. Compared to transparent and stretchable conductors by percolating nanowire networks^{35–38}, our aligned vertical nanowire arrays potentially offers higher surface areas for more charge storages.

Stretchable and transparent supercapacitor

Based on the aforementioned study, we then chose films of t_A , 9 hrs; t_G , 9 mins and t_p , 20 mins as the ideal electrodes to fabricate stretchable and transparent supercapacitor. The proposed stretchable supercapacitor was made by simply producing two layers of such film, sandwiched with a layer of H_2SO_4 -PVA gel electrolyte serving as both separator and electrolyte. A more detailed fabrication method is shown in Methods. The as-received supercapacitors exhibited good transparency during a wide wavelength range from 300 nm to 800 nm, which is 55% at wavelength of 550 nm (Fig. 3a). The second layer of nanorime mesh film contributed mainly the transparency reduction, where electrolyte had negligible influence on transparency. Besides being optically transparent, the supercapacitor prepared is also mechanically flexible which is demonstrated in the inset pictures of Fig. 3a.

Fig. 3b depicts the cyclic voltammetry (CV) curves of a supercapacitor in a wide range of scan rates (10–500 mV/s). The CV curves maintained an ideal, rectangular shape at scan rates of up to 500 mV/s, demonstrating the good electrical double layer capacitive behavior and rate capability of the device. Fig. 3c shows

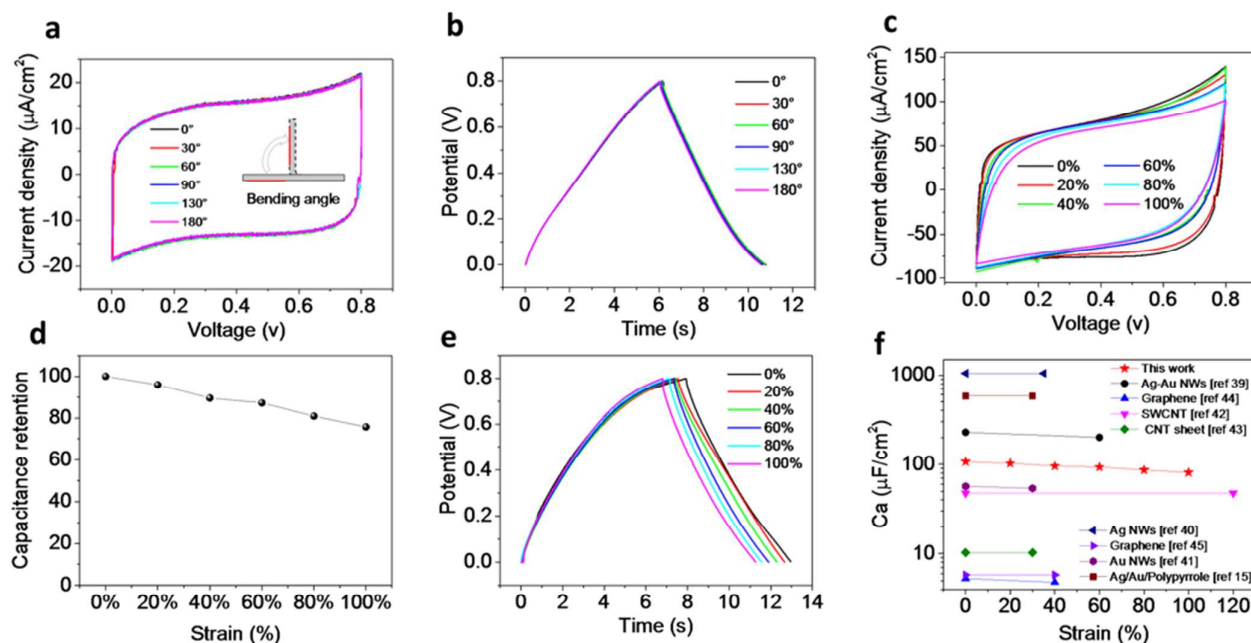


Fig. 4 Capacitance retention under bending and stretching tests. (a) CV curves of the supercapacitor under different bending angle from 0 to 180 degrees. Scan rate is 20 mV/s. (b) GCD curves of the supercapacitor at a constant current of 20 mA, under different bending angle from 0 to 180 degrees. (c) CV curves of the supercapacitor under different strains from 0% to 100%. Scan rate: 600 mV/s. (d) Capacitance retention (%) under different strains from 0% to 100%. (e) GCD curves of the supercapacitor at a constant current of 26.7 mA under different strains from 0% to 100%. (f) A comparison of this work to recent literature in transparent stretchable supercapacitors. Data points are extracted from the following papers: Navy left triangle, silver nanowires (Ag NWs) — the study by Park et al. (40); Dark circle, silver-gold core shell nanowires network (Ag-Au NWs) — the study by Lee et al. (39); Purple circle, gold nanowires (Au NWs) — the study by Cheng et al. (41); Magenta inverted triangle, Single wall carbon nanotubes (SWCNTs) — the study by Gilshteyn et al. (42); Olive diamond, Carbon nanotube sheets (CNT sheets) — the study by Chen et al. (43); Violet right triangle, Graphene — the study by Chen et al. (45); Blue up triangle, graphene—(44); the study by Xu et al; Dark red rectangle, Ag/AuPolypyrrole— the study by Moon et al. (15); red filled star, this study.

galvanostatic charge-discharge (GCD) test at current density from 3.3–50 mA/cm² in the potential range of 0–0.8 V, indicating excellent capacitive behaviors with no obvious IR drop. Fig. 3d–e show the corresponding area-specific capacitances of 176.1, 145.8, 144.2, 142.4, 134.7 and 120.1 μF/cm² and 165.4, 143.8, 141.8, 140.0, 136.7 and 129.4 μF/cm² calculated from CV and GCD curves from Fig. 3b–c. Our supercapacitors were able to achieve a maximum energy density of 2.3 and 3.8 mWh cm⁻³, at a power density of 334.6 and 4043 mW cm⁻³, respectively (Fig. 3f).

Bending tests were firstly undertaken to investigate the mechanical flexibility of the supercapacitor. Remarkably, no capacitance degradation can be seen while bending the supercapacitor to as large as 180 degree, which is well proved by both CV and GCD curves (Fig. 4a–b). Capacitance retention stayed at 100% during the whole bending test from 0–180 degree (Fig. S17a in ESI[†]). Fig. S17b in ESI[†] shows the excellent capacitance retention for the 5,000 bending cycles to 180 degree.

Our transparent supercapacitor also shows excellent stretchability up to 100% strain (see optical images in Fig. S18, ESI[†]). Fig. 4c depicts the CV curves of a nanorime-based supercapacitor at tensile strains of 0% to 100% under a scan rate of 600 mV/s. The reduced areas enclosed by the CV curves at tensile strains from 0% to 100% corresponded to the decreased area-specific capacitances of 106.6, 102.2, 95.4, 92.9, 86.2, and 80.7 μF/cm² (Fig. S19a in ESI[†]). The capacitance can still maintain ~76% under 100% strain (Fig. 4d). This may be attributed to the mesh-like structures which can accommodate deformation without significant cracks. Compared to conventional continuous metal film, we believe nanorimes may deform like accordion fan during the straining process, which can enhance overall stretchability. In addition, nanorime structures can offer higher surface areas than conventional plated metal films, which can accommodate more ions to adsorb. This explains the high stretchability and capacitance achieved in our system.

The superior electrochemical performance of nanorime-based supercapacitor is further demonstrated by conducting GCD measurements in the potential range 0–0.8 V at a current density of 26.7 mA/cm² under stretching range of 0–100% strain (Fig. 4e). It has to be noted that without any further extrinsic structural design, capacitive behavior outperforms those state-of-the-art transparent stretchable supercapacitors such as those based on metal nanowires^{15, 39–41}, carbon-nanotube films^{42, 43} and graphene^{44, 45} (Fig. 4f).

We also examined the electrochemical stability of the transparent stretchable supercapacitor at a tensile strain of 100% using CV measurement at a scan rate of 500 mV/s for 2,000 cycles of stretching/releasing (Fig. S19b in ESI[†]). The CV curves stayed almost the same during the strain cycling, demonstrating the excellent electrochemical stability as the cycle number increased. The capacitance exhibited negligible changes after 2,000 cycles (Fig. S19c in ESI[†]). Slightly increased capacitance was observed at times, which was probably caused by the enhanced contact area after multiple cycling under large strain with interior nanowire arrays available for charged ions to adsorb.

Conclusions

In summary, we present an entirely solution-based strategy to fabricate optically transparent, electrically conductive, mechanically stretchable nanorime mesh conductors using self-assembled nanowire bundled mesh-templated vertically aligned gold nanowires. This simple yet efficient approach enables us to achieve a high transparency up to 90.3%, a sheet resistance as low as $1.7 \pm 0.8 \Omega \text{ sq}^{-1}$, and a mechanical stretchability of >100% strain without extrinsic structural design. This outstanding performance originates from unique hierarchical nanorime structure, consisting of lying-down nanomesh membrane and highly aligned nanowire arrays. This structure offers high electrochemical surface areas allowing for fabrication of transparent and stretchable supercapacitors. The supercapacitor is as thin as ~100 μm yet stretchable up to 100% strain with ~76% capacitance retention. It also shows superior mechanical flexibility under repeated stretching (0–100% strain) and bending (0–180 degree) cycling. In short, nanorime structures are responsible for the high conductivity and high charge-storage capacity; overall mesh structures offer high optical transparency and mechanical stretchability. Their combination explains well the high performance described above. These attributes, in conjunction with high stability and controllability, indicate our high-performance skin-thin, transparent stretchable supercapacitor may become an important component in future unseeable and unfeelable wearable electronics.

Experimental Section

Materials

Gold (III) chloride trihydrate (HAuCl₄·3H₂O, 99.9%), Triisopropylsilane (99%), 4-Mercaptobenzoic acid (MBA, 90%), L-ascorbic acid, Poly (vinyl alcohol) (PVA) powder, H₃PO₄, and ethanol (analytical grade) were purchased from Sigma Aldrich. All solutions were prepared using deionized water (resistivity >18 MΩ·cm⁻¹). All chemicals were used as received unless otherwise indicated. Conductive wires were purchased from Adafruit Industries.

Elastomeric substrates: Polydimethylsiloxane (PDMS) substrates were made by the mixing the Sylgard 184 Silicone Elastomer Base and the Curing Agent at the weight ratio of 10:1. The mixture was poured on a 6" flat-plate petri dish and cured at 65°C for 2 h in an oven. Thin PDMS film, ca 50 μm was obtained by using spinning coating. Polyethylene terephthalate (PET) films (thickness, 40 μm) were used as received.

Preparation of gold nanowire solution (oleylamine-capped)

44 mg HAuCl₄·3H₂O was added into 40 ml hexane, followed by addition of 1.5 ml Oleylamine (OA). 2.1 ml Triisopropylsilane was added into the above solution after completely dissolving the gold salts. The resulting solution was left to stand for 2 days undisturbed at room temperature until the colour turned from yellow into dark, indicating the formation of gold nanowires. The residue chemicals were removed by repeated centrifugations and thorough washing using ethanol/hexane (3/1, v/v). Finally, the nanowire solution was concentrated to a 2 ml stock in hexane. Then storage the as

prepared gold nanowire solution at room temperature for the period of time of interest.

Preparation of gold nanorime mesh transparent conductors

The assembly of well-defined monolayer of gold nanowire mesh structure was achieved using a modified Langmuir–Blodgett technique described previously. The nanowire assemblies were prepared at room temperature in petri dish (3.5 inches) using Millipore Milli-Q water. A 20 ml syringe was used to dispense as-prepared aged gold nanowire solution onto the water subphase, drop by drop. The droplet quickly spread over the water surface and evaporated to leave a gold nanowire mesh membrane fully covered the water surface. After 30 minutes of equilibration, the gold nanowire mesh membranes were transferred onto PDMS substrates by slowly pulling the substrates out of the aqueous subphase. The as-prepared gold nanowire mesh structure on PDMS substrates was exposed to an O₂ plasma treatment for 20 minutes to enable effective aligned nanowire arrays growth on mesh structure. Finally, immerse the as prepared films into nanowire growth solution containing 980 μM MBA, 12 mM H₂AuCl₄, 2.9 mM L-ascorbic acid, leading to the formation of densely aligned nanowire arrays.

Preparation of Supercapacitor

The as prepared transparent electrodes were cut into small pieces with suitable shapes and sizes. A gel solution which contained PVA powder (1.0 g) and H₃PO₄ (1.0 g) in water (10.0 ml) was coated on top of the prepared films and dried them in air for 5 hrs. Then two such-prepared electrodes were assembled with sandwiched electrolytes to form a symmetrical electrochemical capacitor. The active size for supercapacitors is 2 cm by 3 cm.

Characterization

Optical and digital images were recorded by the Nikon ECLIPSE LV150 microscope and Samsung Galaxy S3 smart phone. Optical transmittance was measured by the Agilent 8453 UV–vis spectrophotometer. Scanning Electron Microscopy imaging was carried out using FEI Helios Nanolab 600 FIB-SEM operating at a voltage of 5 kV. The sheet resistances were carried out on a Jandel four point conductivity probe by using a linear arrayed four point head. To test the electro-mechanical responses, the two ends of the samples were attached to motorized moving stages (THORLABS Model LTS150/M). Then uniform stretching/releasing cycles were applied by a computer-based user interface (Thorlabs APT user), while the current changes were measured by the Parstat 2273 electrochemical system (Princeton Applied Research).

Acknowledgements

This work is financially supported by ARC Discovery projects DP180101715 and DP170102208. This work was performed in part at the Melbourne Centre for Nanofabrication (MCN) in the Victorian Node of the Australian National Fabrication Facility (ANFF).

Competing interests

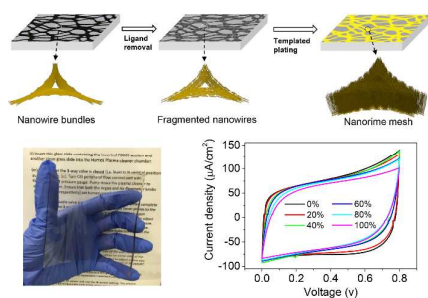
There are no conflicts to declare.

Notes and references

1. J. A. Rogers, T. Someya and Y. Huang, *Science.*, 2010, **327**, 1603-1607.
2. M. D. Ho, Y. Ling, L. W. Yap, Y. Wang, D. Dong, Y. Zhao and W. Cheng, *Adv Funct Mater.*, 2017, **27**, 1700845.
3. S. Gong and W. Cheng, *Adv. Energy. Mater.*, 2017, **7**, 1700648.
4. D. J. Lipomi and Z. Bao, *Energy & Env. Sci.*, 2011, **4**, 3314-3328.
5. S. Xu, Y. Zhang, J. Cho, J. Lee, X. Huang, L. Jia, J. A. Fan, Y. Su, J. Su and H. Zhang, *Nat Commu.*, 2013, **4**, 1543.
6. C. Yu, C. Masarapu, J. Rong, B. Wei and H. Jiang, *Adv Mater.*, 2009, **21**, 4793-4797.
7. Z. Niu, H. Dong, B. Zhu, J. Li, H. H. Hng, W. Zhou, X. Chen and S. Xie, *Adv Mater.*, 2013, **25**, 1058-1064.
8. W. Guo, C. Xu, X. Wang, S. Wang, C. Pan, C. Lin and Z. L. Wang, *Journal of the American Chemical Society.*, 2012, **134**, 4437-4441.
9. J. Chen, Y. Huang, N. Zhang, H. Zou, R. Liu, C. Tao, X. Fan and Z. L. Wang, *Nat Energy.*, 2016, **1**, 16138.
10. L. Liang, C. Gao, G. Chen and C.-Y. Guo, *Journal of Materials Chemistry C.*, 2016, **4**, 526-532.
11. R. Zhang, J. Ding, C. Liu and E.-H. Yang, *ACS Applied Energy Materials.* 2018, **1**, 2048-2055.
12. M. F. El-Kady, V. Strong, S. Dubin and R. B. Kaner, *Science.*, 2012, **335**, 1326-1330.
13. D. Qi, Z. Liu, Y. Liu, W. R. Leow, B. Zhu, H. Yang, J. Yu, W. Wang, H. Wang and S. Yin, *Adv Mater.*, 2015, **27**, 5559-5566.
14. J. Zang, C. Cao, Y. Feng, J. Liu and X. Zhao, *Scientific reports.* 2014, **4**, 6492.
15. H. Moon, H. Lee, J. Kwon, Y. D. Suh, D. K. Kim, I. Ha, J. Yeo, S. Hong and S. H. Ko, *Sci Rep.*, 2017, **7**, 41981.
16. Z. Lv, Y. Luo, Y. Tang, J. Wei, Z. Zhu, X. Zhou, W. Li, Y. Zeng, W. Zhang and Y. Zhang, *Advanced Materials.*, 2018, **30**.
17. H. Lin, L. Li, J. Ren, Z. Cai, L. Qiu, Z. Yang and H. Peng, *Sci Rep.*, 2013, **3**, 1353.
18. G. Wang, L. Zhang and J. Zhang, *Chemical Society Reviews.*, 2012, **41**, 797-828.
19. X. Li, T. Gu and B. Wei, *Nano Lett.*, 2012, **12**, 6366-6371.
20. X. Li and B. Wei, *Nano Energy.*, 2013, **2**, 159-173.
21. H. Feng, Y. Yang, Y. You, G. Li, J. Guo, T. Yu, Z. Shen, T. Wu and B. Xing, *Chemical Commu.*, 2009, 1984-1986.
22. X. Lu, M. S. Yavuz, H.-Y. Tuan, B. A. Korgel and Y. Xia, *Journal of the American Chemical Society.*, 2008, **130**, 8900-8901.
23. S. Gong, Y. Zhao, L. W. Yap, Q. Shi, Y. Wang, J. A. P. B. Bay, D. T. H. Lai, H. Uddin and W. Cheng, *Adv. Electronic. Mater.*, 2016, **2**, 1600121.
24. J. He, Y. Wang, Y. Feng, X. Qi, Z. Zeng, Q. Liu, W. S. Teo, C. L. Gan, H. Zhang and H. Chen, *ACS nano.*, 2013, **7**, 2733-2740.
25. I. Herman, J. Yeo, S. Hong, D. Lee, K. H. Nam, J. H. Choi, W. H. Hong, D. Lee, C. P. Grigoropoulos and S. H. Ko, *Nanotechnology.* 2012, **23**, 194005.

26. S. H. Ko, D. Lee, H. W. Kang, K. H. Nam, J. Y. Yeo, S. J. Hong, C. P. Grigoropoulos and H. J. Sung, *Nano Lett.* 2011, **11**, 666-671.
27. H. Lee, W. Manorotkul, J. Lee, J. Kwon, Y. D. Suh, D. Paeng, C. P. Grigoropoulos, S. Han, S. Hong, J. Yeo and S. H. Ko, *ACS Nano*. 2017, **11**, 12311-12317.
28. H. Lee, J. Yeo, J. Lee, H. Cho, J. Kwon, S. Han, S. Kim, S. Hong and S. H. Ko, *The Journal of Physical Chemistry C*. 2017, **121**, 22542-22549.
29. J. Yeo, G. Kim, S. Hong, J. Lee, J. Kwon, H. Lee, H. Park, W. Manorotkul, M. T. Lee, B. J. Lee, C. P. Grigoropoulos and S. H. Ko, *Small*. 2014, **10**, 5015-5022.
30. A. Sanchez-Iglesias, B. Rivas-Murias, M. Grzelczak, J. Perez-Juste, L. M. Liz-Marzan, F. Rivadulla and M. A. Correa-Duarte, *Nano Lett.*, 2012, **12**, 6066-6070.
31. Y. Chen, Z. Ouyang, M. Gu and W. Cheng, *Adv Mater.*, 2013, **25**, 80-85.
32. J. H. Maurer, L. Gonzalez-Garcia, B. Reiser, I. Kanelidis and T. Kraus, *Nano Lett.*, 2016, **16**, 2921-2925.
33. D. Azulai, T. Belenkova, H. Gilon, Z. Barkay and G. Markovich, *Nano letters.*, 2009, **9**, 4246-4249.
34. D.-H. Kim, N. Lu, R. Ma, Y.-S. Kim, R.-H. Kim, S. Wang, J. Wu, S. M. Won, H. Tao and A. Islam, *Science*. 2011, **333**, 838-843.
35. S. Han, S. Hong, J. Ham, J. Yeo, J. Lee, B. Kang, P. Lee, J. Kwon, S. S. Lee, M. Y. Yang and S. H. Ko, *Adv Mater.* 2014, **26**, 5808-5814.
36. J. Jung, H. Lee, I. Ha, H. Cho, K. K. Kim, J. Kwon, P. Won, S. Hong and S. H. Ko, *ACS Appl Mater Interfaces*. 2017, **9**, 44609-44616.
37. S. Hong, H. Lee, J. Lee, J. Kwon, S. Han, Y. D. Suh, H. Cho, J. Shin, J. Yeo and S. H. Ko, *Adv Mater*. 2015, **27**, 4744-4751.
38. P. Lee, J. Ham, J. Lee, S. Hong, S. Han, Y. D. Suh, S. E. Lee, J. Yeo, S. S. Lee, D. Lee and S. H. Ko, *Advanced Functional Materials*. 2014, **24**, 5671-5678.
39. H. Lee, S. Hong, J. Lee, Y. D. Suh, J. Kwon, H. Moon, H. Kim, J. Yeo and S. H. Ko, *ACS Appl Mater Interfaces.*, 2016, **8**, 15449-15458.
40. S. Park, A. W. M. Tan, J. Wang and P. S. Lee, *Nanoscale Horiz.*, 2017, **2**, 199-204.
41. S. Gong, Y. Zhao, Q. Shi, Y. Wang, L. W. Yap and W. Cheng, *Electroanalysis.*, 2016, **28**, 1298-1304.
42. E. P. Gilshteyn, T. Kallio, P. Kanninen, E. O. Fedorovskaya, A. S. Anisimov and A. G. Nasibulin, *RSC Adv.*, 2016, **6**, 93915-93921.
43. T. Chen, H. Peng, M. Durstock and L. Dai, *Sci Rep.*, 2014, **4**, 3612.
44. T. Chen, Y. Xue, A. K. Roy and L. Dai, *Acs Nano.*, 2013, **8**, 1039-1046.
45. P. Xu, J. Kang, J.-B. Choi, J. Suhr, J. Yu, F. Li, J.-H. Byun, B.-S. Kim and T.-W. Chou, *ACS nano*. 2014, **8**, 9437-9445.

Graphic Table of content:



Supercapacitor with high mechanical stretchability, high optical transparency and high areal capacitance can be achieved simultaneously by using gold nanorime-based mesh electrodes.